Chapter 7

Measuring a granular continuum element

7.1 Introduction

In the previous chapter, it was shown that the Stochastic Flow Rule could extend the applicability of the spot model to other geometries. As the first theory to predict the silo drainage and annular Couette flow from the same underlying principles, it represents a significant advance. However, to achieve this, it made use of the Mohr-Coulomb stresses, and as previously mentioned, there are several aspects of this theory which are troubling, with the theory predicting shocks, even for some simple geometries.

Much of the problem with Mohr-Coulomb Plasticity comes from its treatment of the microscopic element of granular element. As previously described, the additional assumption of Mohr-Coulomb Incipient Yield, stating that the entire packing achieved critical value of μ everywhere, was employed to create a closed system of equations. Ideally, we would like to be able to directly test whether these assumptions about a microscopic granular element are valid.

Recently, a variety of other continuum theories for granular materials have been proposed, which attempt to more precisely capture the underlying physics of a granular element. The Shear Transformation Zones theory developed by Langer *et al.* [43,

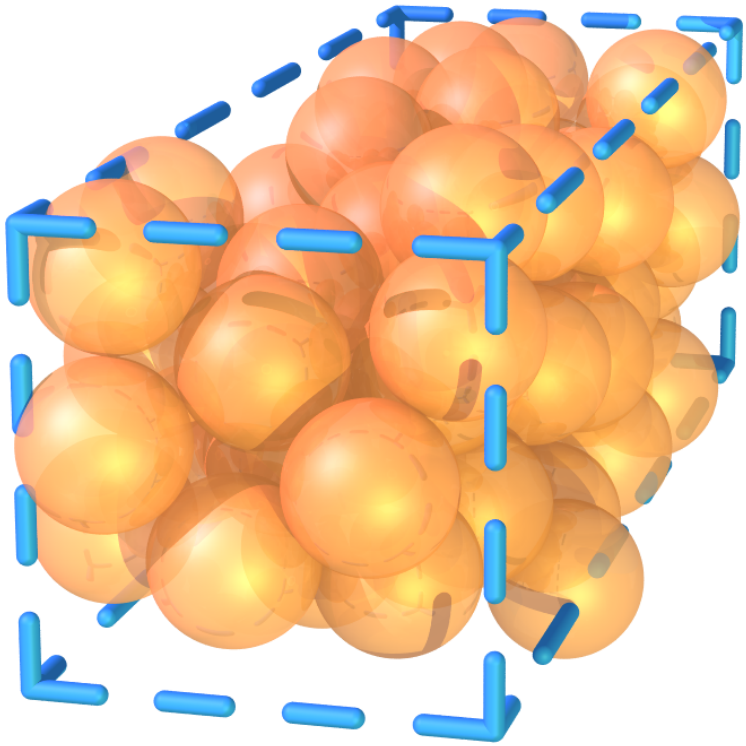

Figure 7-1: A typical $2.5d \times 8d \times 2.5d$ cell of particles from a discrete element method simulation, proposed as an approximate granular element for this study.

75, 73, 74] provides a mechanism for giving granular materials a memory of their shearing history. The partial fluidization model developed by Aranson and Tsimring [8, 9] attempts to separate the solid-like and liquid-like properties of a granular material via an order parameter. From studies of inclined planes, Pouliquen has proposed a flow rule for dense granular flows [62]. However, none of these theories have been developed into a complete continuum description of a granular flow. Like the Mohr-Coulomb theory, additional hypotheses of the granular physics have been employed to create a closed theory, which are then used to generate macroscopic predictions. Testing the macroscopic predictions provides an indirect way to evaluate the original microscopic model.

This chapter demonstrates an alternative approach. Instead of looking at macroscopic properties, we ask the question of whether is possible to directly view and test the properties of a granular element. However, at first sight, it is unclear whether a granular element can be meaningfully defined. In a dense amorphous packing, associ-

ating the notion of a granular element with a single particle appears unclear. As previously noticed, granular materials have complex force networks which are extremely non-homogeneous, with stresses frequently being concentrated on a fractal-like networks of particles. It does not appear that these forces can be directly associated with a continuum notion of stress.

To make progress, we refer back to the results of previous chapters. In chapter 3 it was shown that even with an approximate random-walk model of granular flow, it was possible to generate realistic flowing random packings via the spot mechanism. It suggests that we may only need a physical model to be valid down to the scale of a spot, since the spot model microscopic mechanism will always be able to correct the microscopic packing statistics at the local level. This motivates the definition of a granular element on a mesoscopic length scale, as shown in figure 7-1. Notions of a continuum variables at a single particle level may not make sense, but at the mesoscopic scale, it is possible that they can be defined statistically.

To test this, large-scale DEM simulations were carried out in a variety of dense granular flows. For simplicity, attention to was restricted to quasi-2D flows, where one dimension is periodic with period $8d$, but this still allows for the consideration of a fully three dimensional stress tensor. For each simulation considered, the flow was divided into mesoscopic granular elements, on the scale of $2.5d \times 8d \times 2.5d$, and material quantities were computed for each of these elements. The primary aim has been to show that an approximate granular continuum element can be defined at this scale. Once this is established, the data has been used to test and develop some of the fundamental ideas behind continuum granular flow theories at the local level, by viewing the simulations as an ensemble of approximate granular elements.

7.2 DEM Simulation

Since our overall aim was to extract information about the inherent properties of a granular material, and not its behavior in a particular situation, we considered a variety of different DEM simulations, with different geometries and forcings. To

minimize the effects of elastic modes in the DEM simulations, the Hookean contact model was employed.

Our initial particle packings were generated using a pouring process. We considered a tall silo with base at $z = 0$ and walls at $x = \pm 25d$, and poured in 55,000 particles from $z = 160d$ at a constant rate of $123\tau^{-1}$ to fill the silo to an approximate height of $z = 114d$. We also considered a wide silo, with walls at $x \pm 75d, z = 0$, and poured in 100,000 particles from $z = 160d$ at a constant rate of $379\tau^{-1}$, making a packing up to approximately $z = 69d$. For both situations, the initial packing fraction is approximately 63.5%.

In some situations considered, flow occurs passively in response to gravity. However, we also considered several situations using an external force. In all these cases, this was done by freezing certain particles (so that all forces and torques were zeroed) and then moving them at a constant velocity. For the initial study, three geometries were considered:

- Drainage from the tall silo, through a $6d$-wide slit in the center of the base.
- Drainage from the wide silo, through a $6d$-wide slit in the center of the base.
- Deformation of the wide silo by pushing, created by freezing all particles with centers initially satisfying $z < 7.5d$, and then moving those with $x > 0$ upwards at a constant speed of $0.2d\tau^{-1}$.

In addition, two simulations were carried out to investigate the effect of arresting a developed flow:

- Stopping drainage in the wide silo, by plugging the hole after 50τ.
- Stopping the pushing deformation after 25τ, when the right side of the packing been raised by $5d$.

Finally, to investigate the precise role of strain and strain rate, we considered one additional simulation:

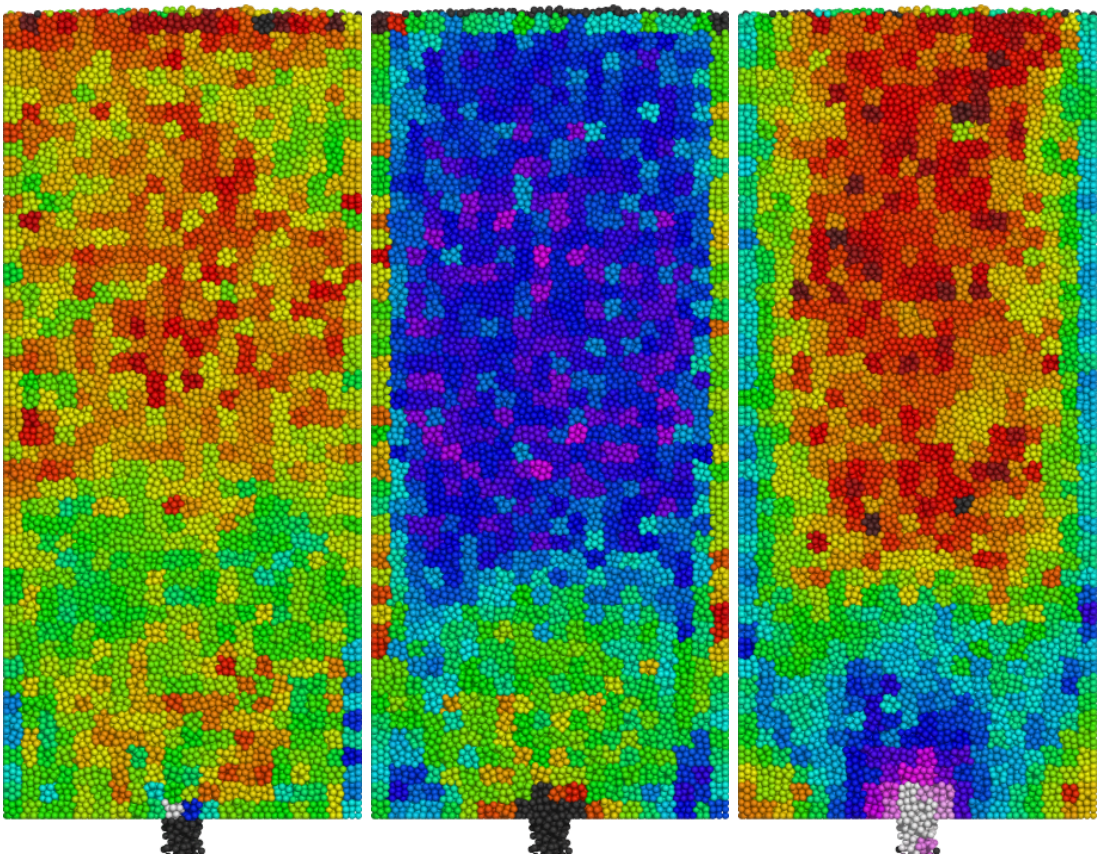

Figure 7-2: Three computed material quantities (μ, packing fraction ϕ, and magnitude of deviatoric strain rate $|\mathbf{D_0}|$) in the tall silo drainage simulation, shown at $t = 25\tau$. All the particles in each computational cell are colored according to the computed material parameters for that cell, using the color scheme of figure 7-3.

- Shearing the wide silo, by freezing all particles whose centers lie within $5d$ of any wall, and then moving those with $x \lesseqgtr 0$ with a velocity of $\pm 0.5 d\tau^{-1}$ in the x direction.

7.3 Computation of material parameters

For each simulation, a snapshot of all particle positions was recorded at fixed intervals of 0.2τ. In addition to this information, numerous material quantities were calculated in a grid of cells of size $2.5d \times 8d \times 2.5d$, and the precise details of these measurements are described below.

As discussed in chapters 4 and 5 we have previously computed local packing frac-

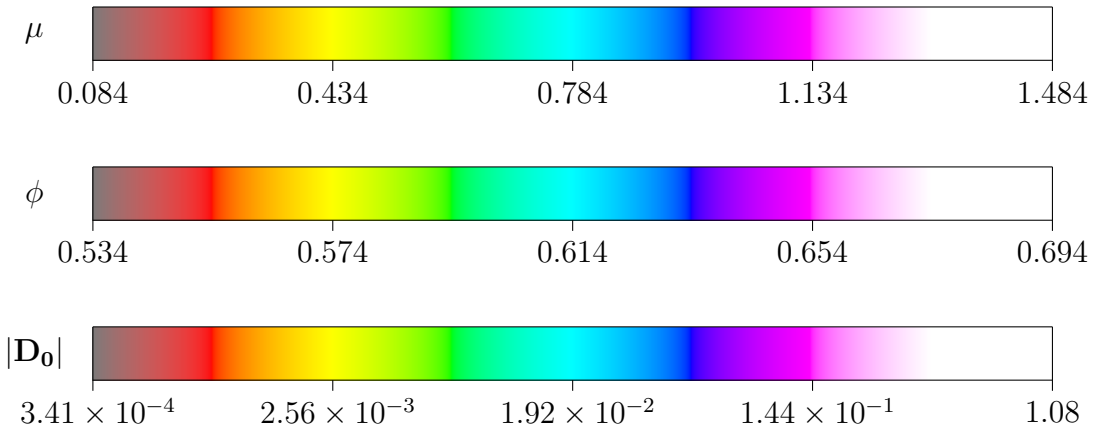

Figure 7-3: Color scheme for the quantities plotted in figures 7-2, 7-4, 7-5, and 7-12. μ and ϕ are dimensionless quantities, while $|\mathbf{D_0}|$ has units of τ^{-1}.

tion using a Voronoi cell method. However, for reasons of computational convenience, we computed it in each cell by evaluating the precise fraction of the cell volume which is occupied by particles. Particles which lie across the boundary of the cell make a fractional contribution, which provides much higher accuracy than only counting particles whose centers lie in the cell. Since the cell is periodic in the y direction, the two cases that must be considered are when the particle intersects a face or edge of the box. Consider a sphere defined by $x^2 + y^2 + z^2 < d^2$. By elementary integration, the proportion of the sphere's volume in the region $x < a$ is

$$\frac{(2d-a)(d+a)^2}{4d^3}$$

It can also be shown that the proportion of the sphere in the region $x < a, y < b$ (where $a^2 + b^2 < d^2$) is

$$\begin{aligned}
&\frac{2ab\sqrt{d^2-a^2-b^2}}{3d^3} \\
&+\frac{b}{d^3}\left(d^2-\frac{b^2}{3}\right)\left(\sin^{-1}\left(\frac{a}{\sqrt{d^2-b^2}}\right)+\frac{\pi}{2}\right) \\
&+\frac{a}{d^3}\left(d^2-\frac{a^2}{3}\right)\left(\sin^{-1}\left(\frac{b}{\sqrt{d^2-a^2}}\right)+\frac{\pi}{2}\right) \\
&+\frac{1}{3}\left(\sin^{-1}\left(\frac{d^4-(a^2+b^2)d^2-a^2b^2)}{(b^2-d^2)(a^2-d^2)}\right)+\frac{\pi}{2}\right).
\end{aligned}$$

The stress tensor in each cell is calculated by looking at the forces between particles in contact. If there are N particles in the cell, and particle l has a total of N_l contacts, then an approximate stress tensor can be defined by

$$T_{ij} = \frac{1}{V} \sum_{l=1}^{N} \sum_{k=1}^{N_l} \Delta x_i^{(k,l)} F_j^{(k,l)}$$

where $\mathbf{F}^{k,l}$ is the force of the kth contact on particle l, and $\mathbf{\Delta x}$ is the separation vector from the point of center of the particle to the point of contact. V is the volume of the cell, and ensures that the stress tensor has the correct units of energy per unit volume, or equivalently force per unit area. This definition is appropriate for a single particle, and taking the average over many particles improves accuracy. This definition of T_{ij} is not explicitly symmetric, but it can be shown that it is approximately symmetric, by considering torques. The total torque on a particle, obtained by summing over all contacts, must add up to the particle's rotational inertia times the particle's angular acceleration. Since the rotational inertia is proportional to d^2, and the particle radius is supposed to be a differentially small quantity, the sum of torques must approach zero. By considering th kth component of torque, we see that

$$\begin{aligned} 0 &\approx \sum_{l=1}^{N} \sum_{k=1}^{N_l} \epsilon_{ijk} x_i^{(k,l)} F_j^{(k,l)} \\ &= \epsilon_{ijk} \sum_{l=1}^{N} \sum_{k=1}^{N_l} x_i^{(k,l)} F_j^{(k,l)} \\ &= \epsilon_{ijk} T_{ij} \end{aligned}$$

and thus $\mathbf{T}$ is approximately symmetric. From this, we can define a pressure $p = \frac{1}{3} \operatorname{tr} \mathbf{T}$ and a deviatoric stress tensor $\mathbf{T_0} = T - \frac{1}{3} p \mathbf{I}$.

In this chapter, we have a fully three-dimensional stress tensor, and thus the simple definition of μ as shear stress divided by normal stress employed in chapter 6 is no longer appropriate. There are three stress directions, with eigenvalues $\lambda_1 < \lambda_2 < \lambda_3$, and from this several definitions of μ exist, two of which are:

- **Drucker-Prager:** For this definition, the normal stress is identified with the

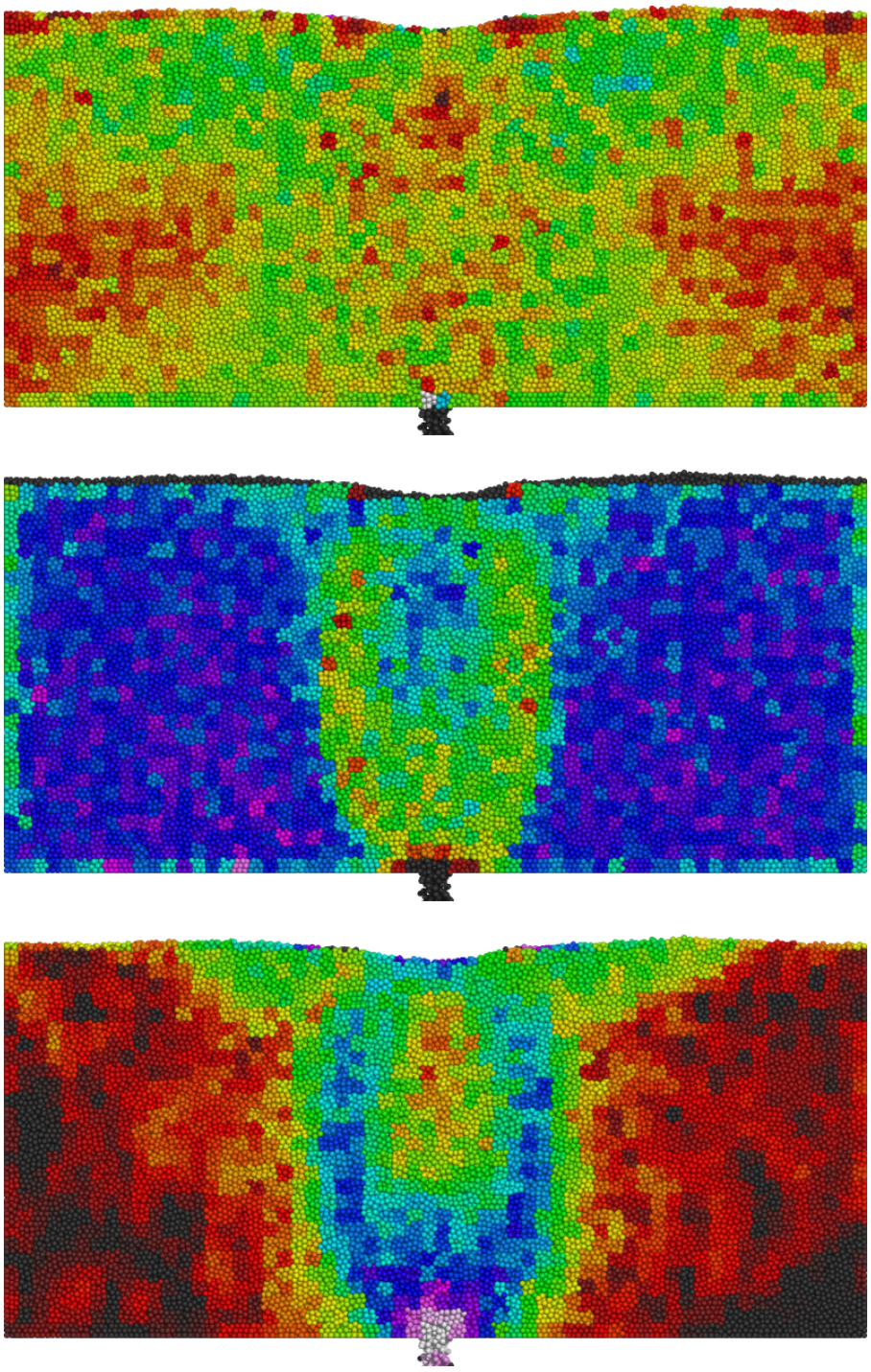

Figure 7-4: Three computed material quantities (μ, top; packing fraction ϕ, middle; magnitude of deviatoric strain rate $|\mathbf{D_0}|$, bottom) in the wide silo drainage simulation at $t = 40\tau$, using the color scheme in figure 7-3.

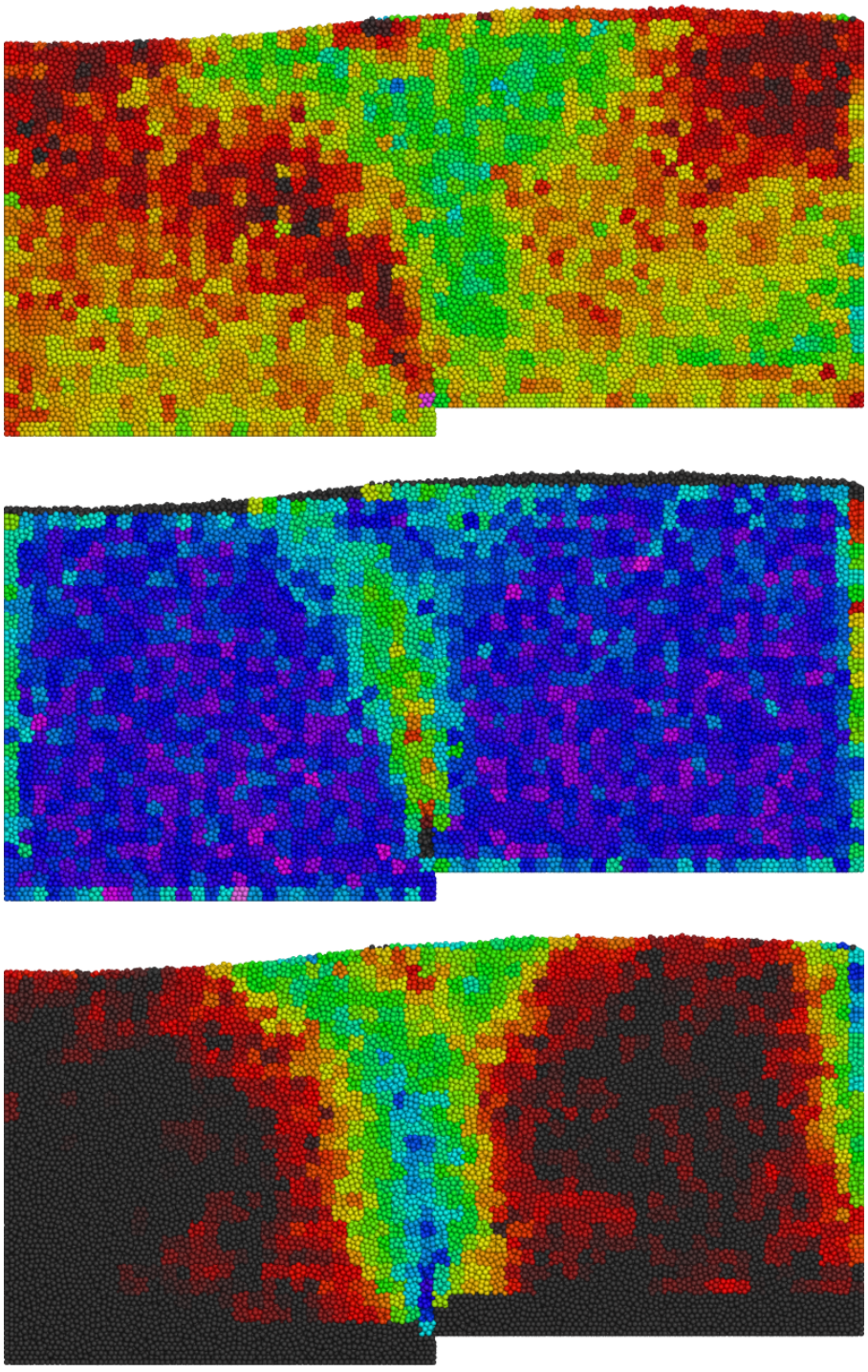

Figure 7-5: Three computed material quantities (μ, top; packing fraction ϕ, middle; magnitude of deviatoric strain rate $|\mathbf{D_0}|$, bottom) in the wide silo pushing simulation at $t = 25\tau$, using the color scheme in figure 7-3.

pressure p, and the shear stress is identified with the magnitude of $\mathbf{D_0}$, divided by a normalizing factor $\sqrt{2}$, so that

$$\mu = \frac{|\mathbf{D_0}|}{p\sqrt{2}}.$$

In terms of the eigenvalues, we have $p = (\lambda_1 + \lambda_2 + \lambda_3)/3$ and

$$\mu = \frac{\sqrt{(\lambda_1 - p)^2 + (\lambda_2 - p)^2 + (\lambda_3 - p)^2}}{p\sqrt{2}}.$$

- **Mohr-Coulomb:** For this definition, the intermediate stress λ_2 is treated as irrelevant, and μ is based on a two-dimensional computation in the plane of the minimal and maximal stresses, where there is an effective stress tensor

$$\mathbf{T}_{\text{eff}} = \begin{pmatrix} \lambda_1 & 0 \\ 0 & \lambda_3 \end{pmatrix}.$$

Rotating the stress tensor by 45° gives

$$\mathbf{T}'_{\text{eff}} = \frac{1}{2}\begin{pmatrix} \lambda_1 + \lambda_3 & \lambda_1 - \lambda_3 \\ \lambda_3 - \lambda_1 & \lambda_1 + \lambda_3 \end{pmatrix}.$$

In this form, we can see that it makes sense to define a normal stress as $p_{\text{eff}} = \operatorname{tr} T = (\lambda_1 + \lambda_3)/2$ and a shear stress as $(\lambda_3 - \lambda_1)/2$. Thus we can define

$$\mu = \frac{\lambda_3 - \lambda_1}{\lambda_3 + \lambda_1}.$$

It was found that both definitions of μ would give reasonable results, although it did appear that in many situations, the value of the intermediate stress had little effect, and thus for the results presented here, the Mohr-Coulomb definition was adopted. Although the stress tensors computed here were fully three-dimensional, they are strongly constrained due to the periodicity in the y direction, and a more in-depth study of the merits of the two definitions would be better carried out in fully three

dimensional, non-periodic systems where there would be greater variations in the stress tensor.

To calculate the strain rate tensor in a cell, we consider the least squares regression problem

$$\mathbf{v} = \mathbf{M}\mathbf{x} + \mathbf{v}^0.$$

Here $\mathbf{x}$ and $\mathbf{v}$ are the instantaneous positions and velocities of all particles within the cell. We find the average cell velocity $\mathbf{v}^0$ and the velocity gradient by minimizing the sum of squares of residuals. Since the simulation is periodic in the y direction, we enforce that the second column of M is zero, as the velocity should not have an explicit dependence on the periodic coordinate. Note however that the velocity in the y direction does play a role, and the elements M_{21}, M_{23} are allowed to be non-zero, and may, for example, be significant in the shearing simulation. The regression problem can be broken down into three separate equations each of which has three parameters, M_{i1}, M_{i3}, and v_i^0. The parameter v_i^0 can be expressed in terms of the means of the $\mathbf{x}$ and $\mathbf{v}$, leaving two components in M for each equation. This can be solved algebraically, without any need to result to a linear matrix solver. The strain rate tensor is then defined as the symmetric part of M, namely

$$\mathbf{D} = \frac{\mathbf{M} + \mathbf{M}^{\mathrm{T}}}{2}.$$

From this, the deviatoric strain rate tensor is defined as $\mathbf{D_0} = \mathbf{D} - \frac{1}{3}(\operatorname{tr}\mathbf{D})\mathbf{I}$. In most cases we expect $\mathbf{D_0} \approx \mathbf{D}$ since the density of the granular material does not fluctuate by a large amount, making the contribution to $\mathbf{D}$ from shearing larger than that from dilation. For some of the analysis, we made use of a normalized strain rate $|\mathbf{D_0}|/\sqrt{p}$. For the results presented here, we used instantaneous particles velocities throughout. However, since these instantaneous quantities may be subject to simulation artefacts, such as particle rattling, or elastic modes, we also considered calculating strain rate based on velocities computed by interpolating between particle positions between successive frames, effectively giving an averaged velocity on the scale of 0.2τ. A plot of $\log|\mathbf{D_0}|$ for the two different computation methods appears linear to a high degree

of accuracy, indicating little physical distinction between them.

7.4 Stress, strain rate and packing fraction

Figure 7-2 shows plots of the Mohr-Coulomb parameter μ, the local packing fraction ϕ, and the magnitude of deviatoric strain rate $|\mathbf{D_0}|$ for the tall silo drainage simulation. Near the orifice, there is a converging region of flow, that has roughly parabolic streamlines. Higher in the container, there is a transition to uniform flow, where the particles drop like a plug, behave like a solid, and experience little rearrangement. The plot of $|\mathbf{D_0}|$ supports these results. High in the container, very little rearrangement is seen, while there is a sharp transition to high values when the packing must undergo deformation to pass through the orifice.

It is clear from looking at the plot of local packing fraction, that ϕ and $|\mathbf{D_0}|$ are closely correlated. In the upper region, where particles are falling like a plug, the packing fraction remains constant. In the converging region, the packing fraction decreases, as the particles must have more free space in order to geometrically rearrange. This verifies the well-known concept of shear-dilation, and is studied quantitatively in later sections.

Of the three plots, μ exhibits the largest fluctuations, which we attribute to the fact that it is a ratio between two computed quantities. However, large variations over the range 0.2 to 0.6 can be clearly seen. This immediately calls the Mohr-Coulomb incipient yield hypothesis into question, which would predict that μ would be constant everywhere, achieving a value of approximately 0.45 to 0.55. At first sight, the spatial differences in μ appear confusing, and not directly correlated with the other two plots. However, regions of higher μ exist at the interface between the plug-like region, and the converging flow region, suggesting that a large μ my be required in order to first achieve material failure; this point will be expanded on in section 7.5.

Figures 7-4 and 7-5 show the same three plots for the wide drainage and wide pushing simulations. Although these are different situations, a number of the same conclusions can be drawn. Again, we see a clear differentiation between solid-like

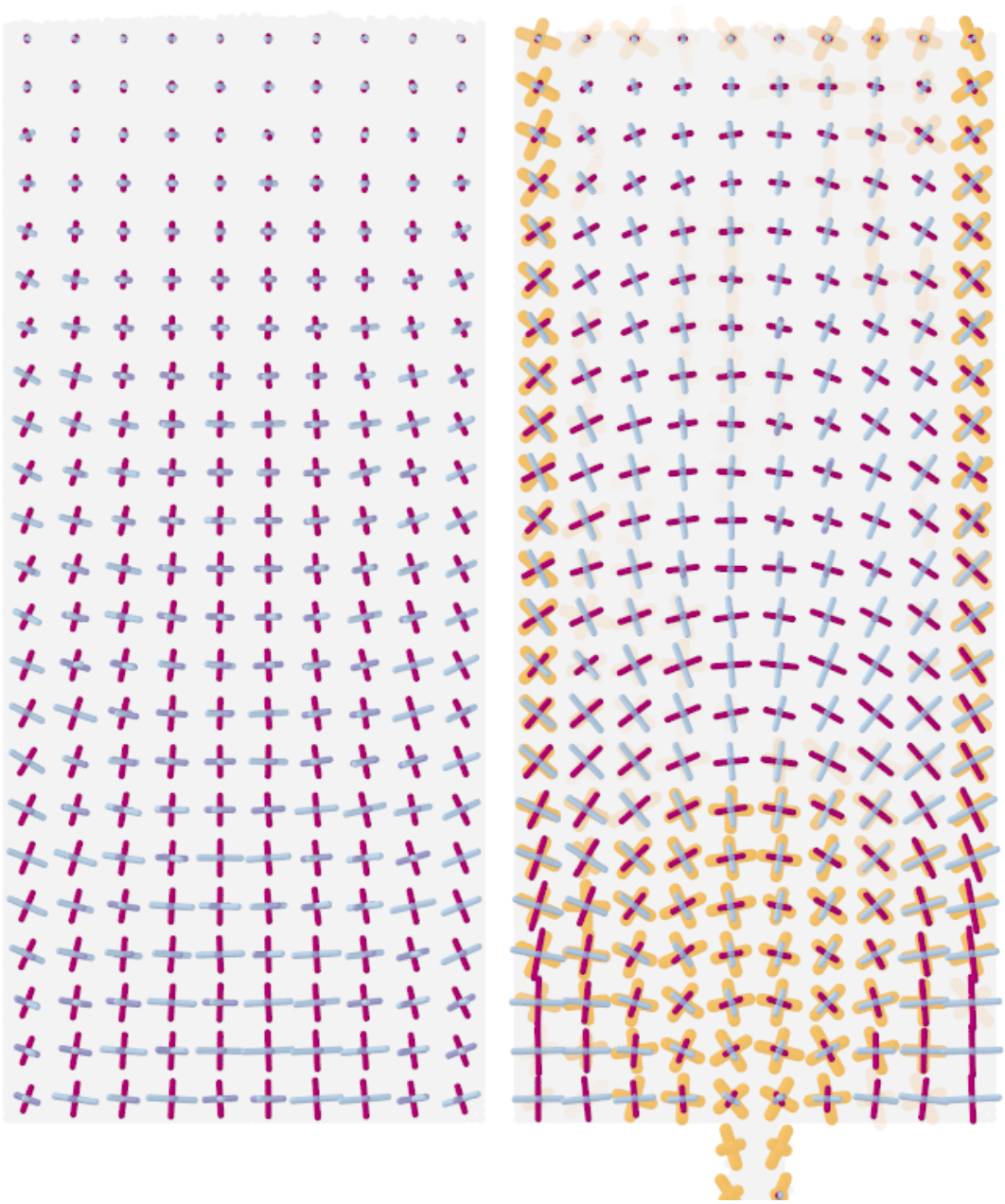

Figure 7-6: Plots of the directions and magnitudes of the eigenvectors of the deviatoric stress and strain rate tensors, calculated instantaneously in $5d \times 8d \times 5d$ boxes with no time-averaging, for the tall silo before drainage (left), and during drainage (right). The maximal stress eigenvector is shown in purple, with the other two eigenvectors being shown in blue. In the regions where deformation is occurring, the maximal and minimal eigenvectors of the strain rate tensors are plotted in orange. A high degree of alignment between the two tensors can be seen.

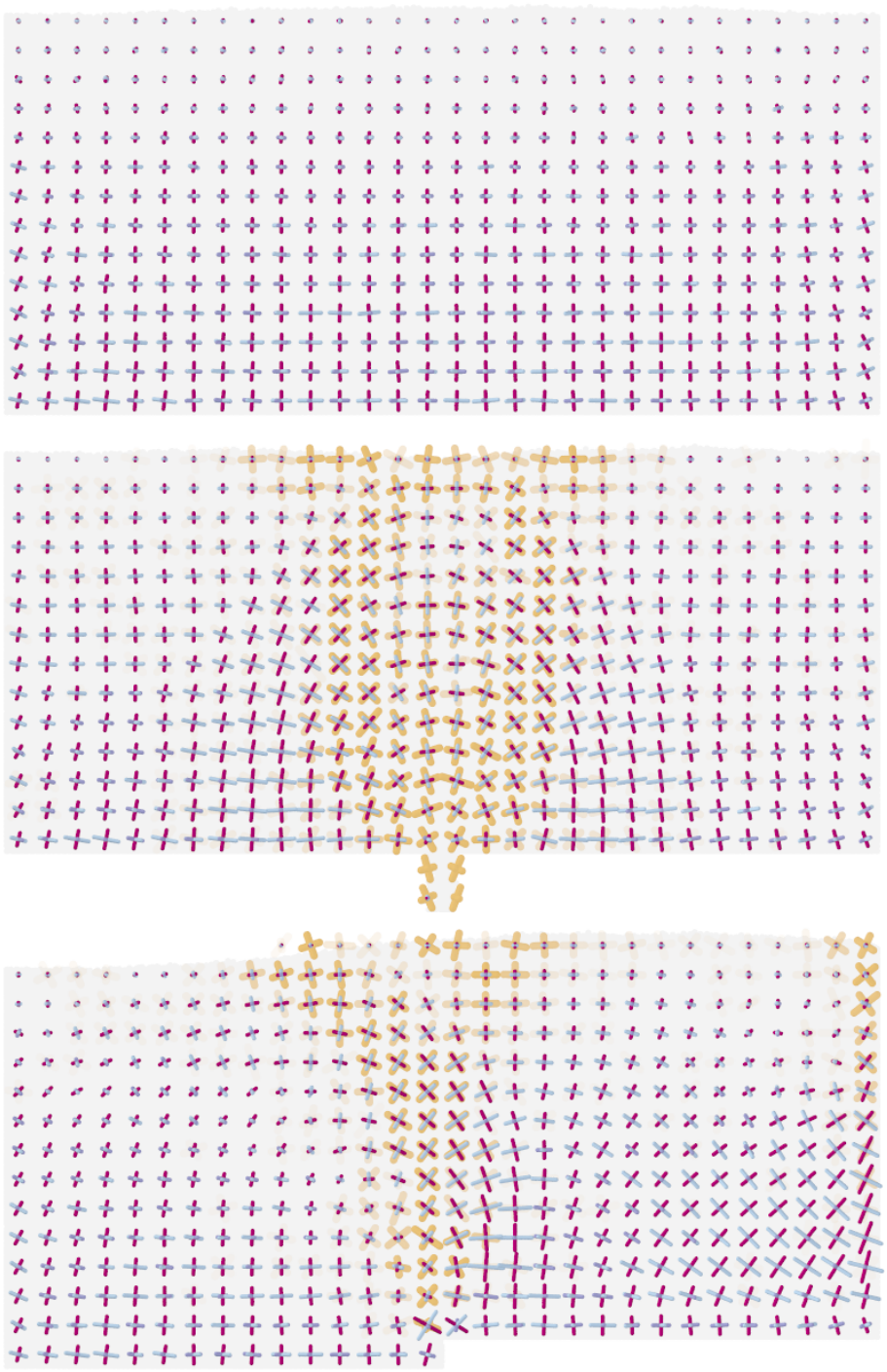

Figure 7-7: Plots of the directions and magnitudes of the eigenvectors of the deviatoric stress and strain rate tensors, calculated instantaneously in $5d \times 8d \times 5d$ boxes with no time-averaging, shown for the initial packing (top), during drainage (middle), and during pushing (bottom). The same color scheme is used as in figure 7-6. Again, a high degree of alignment between the two tensors can be seen.

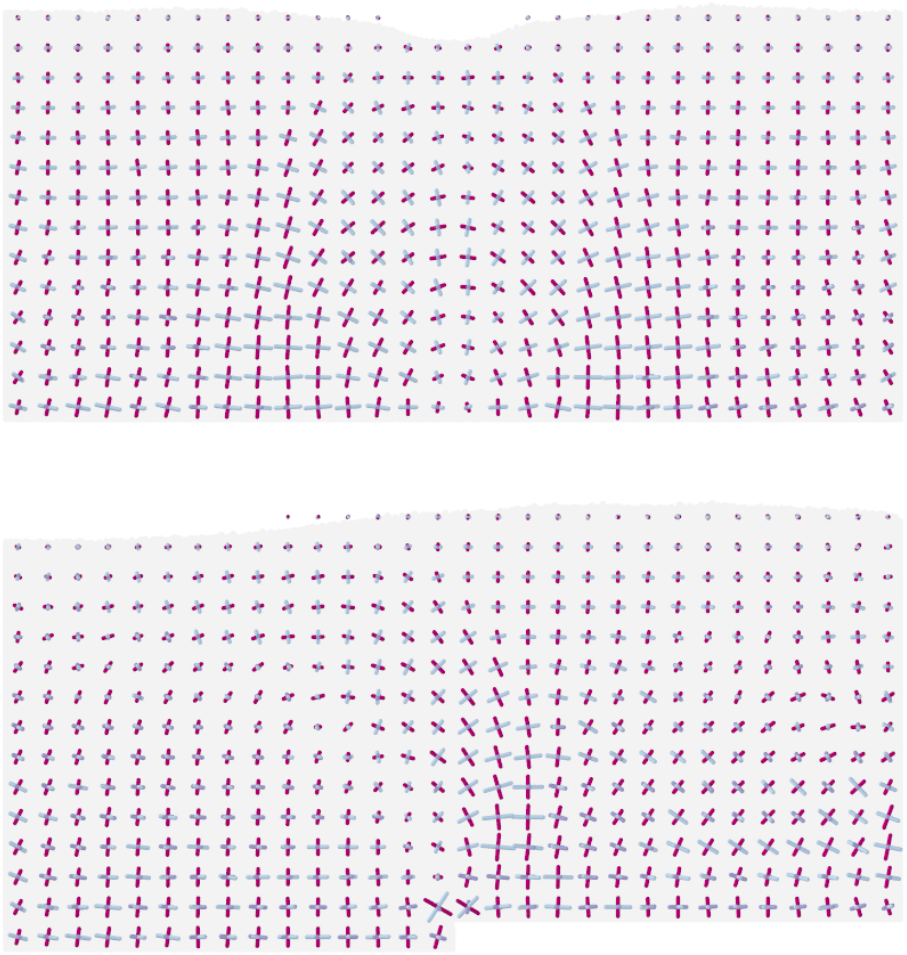

Figure 7-8: Plots of the directions and magnitudes of the eigenvectors of the deviatoric stress tensors, calculated instantaneously in $5d \times 8d \times 5d$ boxes with no time-averaging, after the drainage (left) and pushing processes were arrested. The same color scheme is used as in figure 7-6. The stress lines closely resemble the stress lines during the corresponding flowing states.

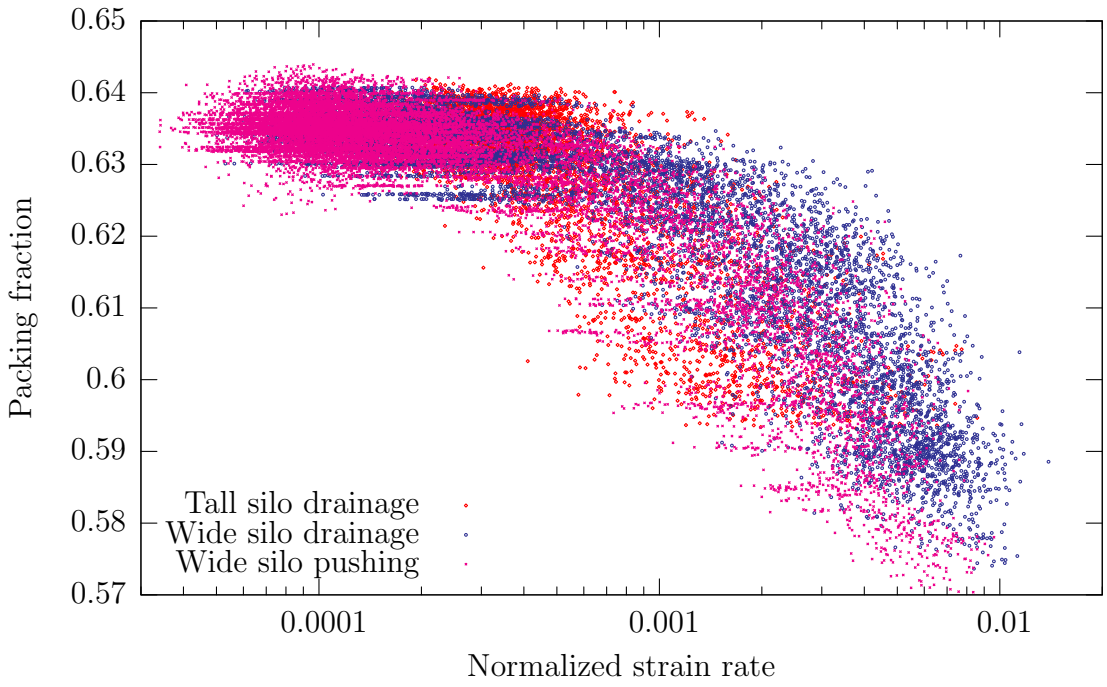

Figure 7-9: Normalized strain rate versus packing fraction for three different simulations. Each point corresponds to the strain rate and packing fraction of a computational cell at a particular instant. The results for computational cells next to the walls exhibit more complex behavior and are not included.

regions with low strain rate and high packing fraction, and liquid-like regions with high strain rate and low packing fraction. Again, the regions of highest μ appear to be at the interfaces between the solid-like and liquid-like regions. Since these correlations hold locally across a variety of different experimental geometries, it gives us reason to believe that they tell us something inherent about the granular material, that is not tied to a particular geometry.

Figures 7-6 and 7-7 show the directions and magnitudes of the eigenvectors of the deviatoric stress tensor for three different simulations, compared with their initial states. For these images, the stress tensor was calculated on a $5d \times 8d \times 5d$ grid, by averaging the computed stress tensor in 2×2 blocks of cells. Even though these stresses were computed using local, instantaneous data, we can see that in all situations, the stress tensors are smooth, and exhibit none of the shocks predicted by plasticity theory. For regions undergoing deformation, the eigenvectors of the strain rate tensor are also shown. We see that in all areas where there is appreciable strain

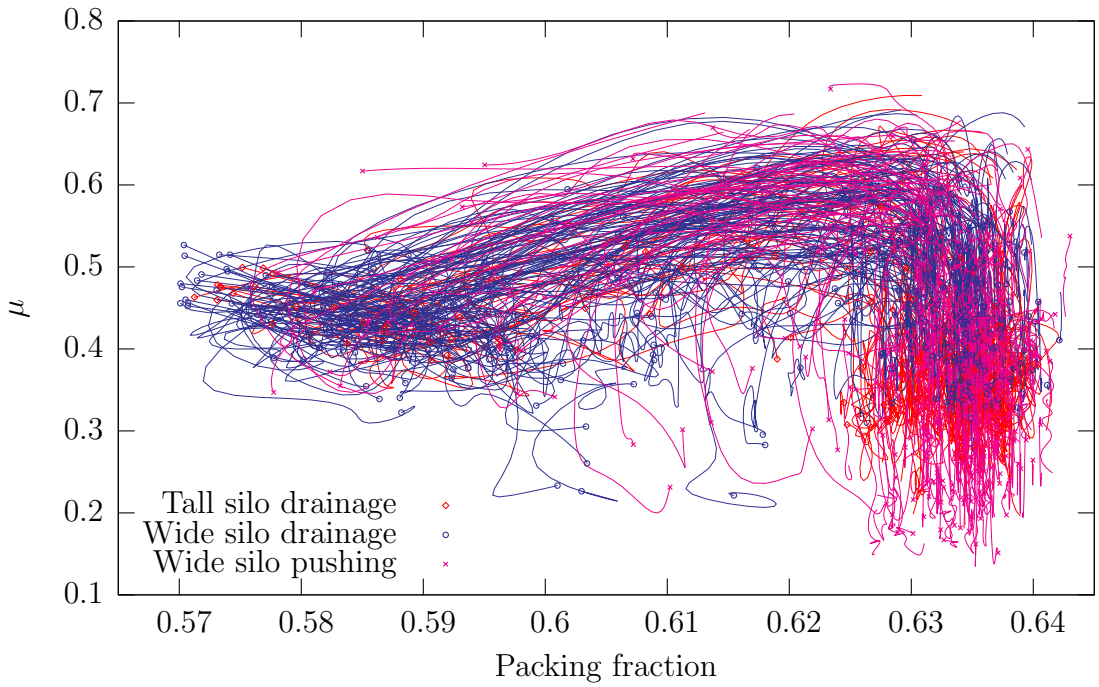

Figure 7-10: Packing fraction versus μ for three different simulations. Each line corresponds to the history of a granular element being advected during the flow of the material. The points which are plotted correspond to the end of the tracers. The tracers' trajectories are Gaussian-smoothed over a time scale of twenty frames to improve accuracy.

rate, there is a strong alignment between the two sets of eigenvectors, even at the local, instantaneous level. If the plots are time-averaged over a window of twenty frames, then the agreement becomes almost perfect. Averaging over progressively larger time windows also allows us to verify coaxiality as far into the granular packing as one can reasonably define a strain rate tensor. These results suggest that while the solid-like/liquid-like distinction is useful, it may be that the concept of liquid-like only makes sense when coupled with an appropriate time window.

In the two wide simulations, the flow process was arrested, and the resulting stress tensors are shown in figure 7-8, The stresses during flow essentially frozen in place, apart from small variations, presumably due to the fact that the material's weight must be redistributed as the packing alters from flowing to static. The stress lines showed no indication of reverting back to their initial state.

7.5 Evolution of material parameters

The plots shown in figures 7-2, 7-4, and 7-5 suggest that a number of correlations exist between the various material parameters at the local level. In this section we investigate these correlations in detail, by viewing all the material cells from the different experiments as an ensemble of approximate "granular elements". Seeking statistical signatures of the material parameters over the ensemble allows us to infer the behaviour of a granular element.

As a first example, consider figure 7-9(a), showing a plot of normalized strain rate $|\mathbf{D_0}|/\sqrt{p}$ against packing fraction. Each point on the graph corresponds to the instantaneous computed values of a material element from one of the simulations, during a period when steady flow has developed. We see an approximate collapse of the points from the three simulations, suggesting that the correlation we are viewing is a property inherent to the granular material, and not tied to any particular simulation configuration. This result has been observed by other authors, such as in the two dimensional simulations of da Cruz *et al.* [33], but we believe this is the first direct verification in three dimensions, at the local level.

While instructive, the above approach will only allow us to search for direct correlations between variables. In reality, we expect that the material parameters are related in a more complicated way, and that differential relationships may exist. Furthermore, we expect that each granular element may have a "memory", and that there may be internal degrees of freedom which we are not measuring, which relate to its history of deformation and stress. Because of these complications, it is natural to switch from an Eulerian to Lagrangian approach: rather than viewing our data set as an ensemble of over different spatial positions and times, we treat it as an ensemble of different spatial elements which evolve over time. Each granular element corresponds to an approximate trace in the phase space of material parameters over its history during the simulation.

To correctly implement this, we must also take into account that a granular cell may move during the simulation. We therefore initially introduced a number of tracer

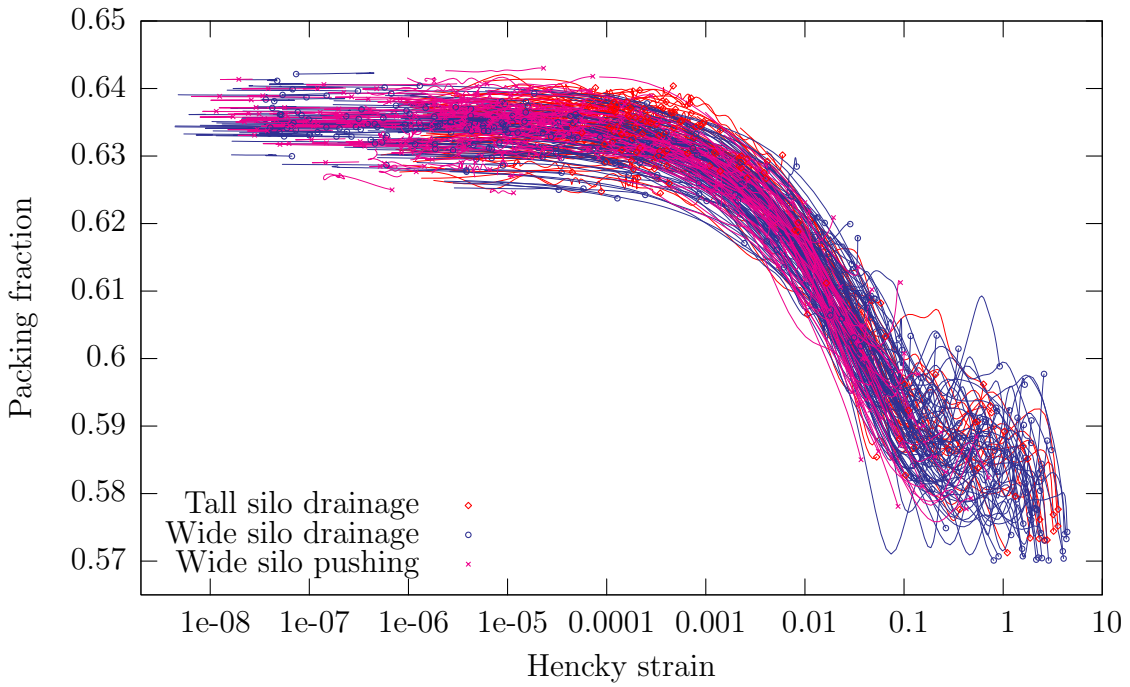

Figure 7-11: Strain versus packing fraction for three different simulations. Each line corresponds to the history of a granular element being advected during the flow of the material. The points which are plotted correspond to the end of the tracers. The tracers' trajectories are Gaussian-smoothed over a time scale of twenty frames to improve accuracy.

positions on a $5d \times 5d$ lattice. During the simulation, the tracer positions are advected according the average background velocity of the particles. For each tracer, a history of a granular element is created by linearly interpolating all the material parameters from the underlying raw simulation data on the $2.5d \times 2.5d$ lattice.

Figure 7-9 shows sample of tracers in a plot of μ against packing fraction ϕ. The plot shows us that, while μ is not directly correlated to ϕ, it plays an important role in the failure of a granular element. The majority of tracers start off on the right side of the graph, at the initial packing fraction of 63.5%. Those tracers corresponding to failing elements take a path in an inverted U-shape, first attaining a value of μ of approximately 0.55 before starting to decrease in packing fraction. A material element will dilate only if a critical value of μ is first attained. This directly relates to the behavior seen in figures 7-2, 7-4, and 7-5, where it was noted that areas of larger μ were located at the interface between solid-like and liquid-like regions. Also

visible in 7-10 is tendency for dilated elements which experience a low value of μ to recompact slightly, suggested by the fact that the majority of the paths in the lower left portion of the graph are moving rightwards.

In the Lagrangian approach it also makes sense to consider the total strain experienced by a material element. Strain is calculated from the simulation data by using the snapshots of all particle positions. At $t = 0$, a $5d \times 8d \times 5d$ box of particles is labeled, centered on each material tracer. Let $\mathbf{x}^i$ be the initial particle positions in a particular box. A deformation gradient tensor $\mathbf{F}$ and an overall drift $\mathbf{x}^0$ can then be found by considering the least squares regression problem

$$\mathbf{x} = \mathbf{F}\mathbf{x}^i + \mathbf{x}^0$$

where $\mathbf{x}$ are the current particle positions. Due to the periodicity, we enforce that $M_{12} = M_{32} = 0$, and $M_{22} = 1$. This problem is very similar to the previous calculations of a deformation tensor, and can be done analytically. We can then compute a polar decomposition $\mathbf{F} = \mathbf{R}\mathbf{U}$ where $\mathbf{R}$ is a rotation matrix, and $\mathbf{U}$ is a symmetric positive definite matrix. The concept of a strain is not well-defined, and from $\mathbf{U}$ there are several ways to define strain-like quantity. For the work presented here, we make use of the Hencky strain $\mathbf{E} = \log \mathbf{U}$, which has the additional property that strains are additive. However, this choice is arbitrary, and the same conclusions could be drawn from any of the other definitions.

Figure 7-11 shows a plot of strain against packing fraction for the three simulations. Again, we see a very clear collapse, perhaps even better than the plot for strain rate. This will be developed in the following section.

7.6 The precise mechanism of shear dilation

Figure 7-9 suggested a strong correlation between strain rate and packing fraction in the three simulations, and this has been observed by other authors in the physics community. However, in figure 7-11, we saw a clear correlation between strain and

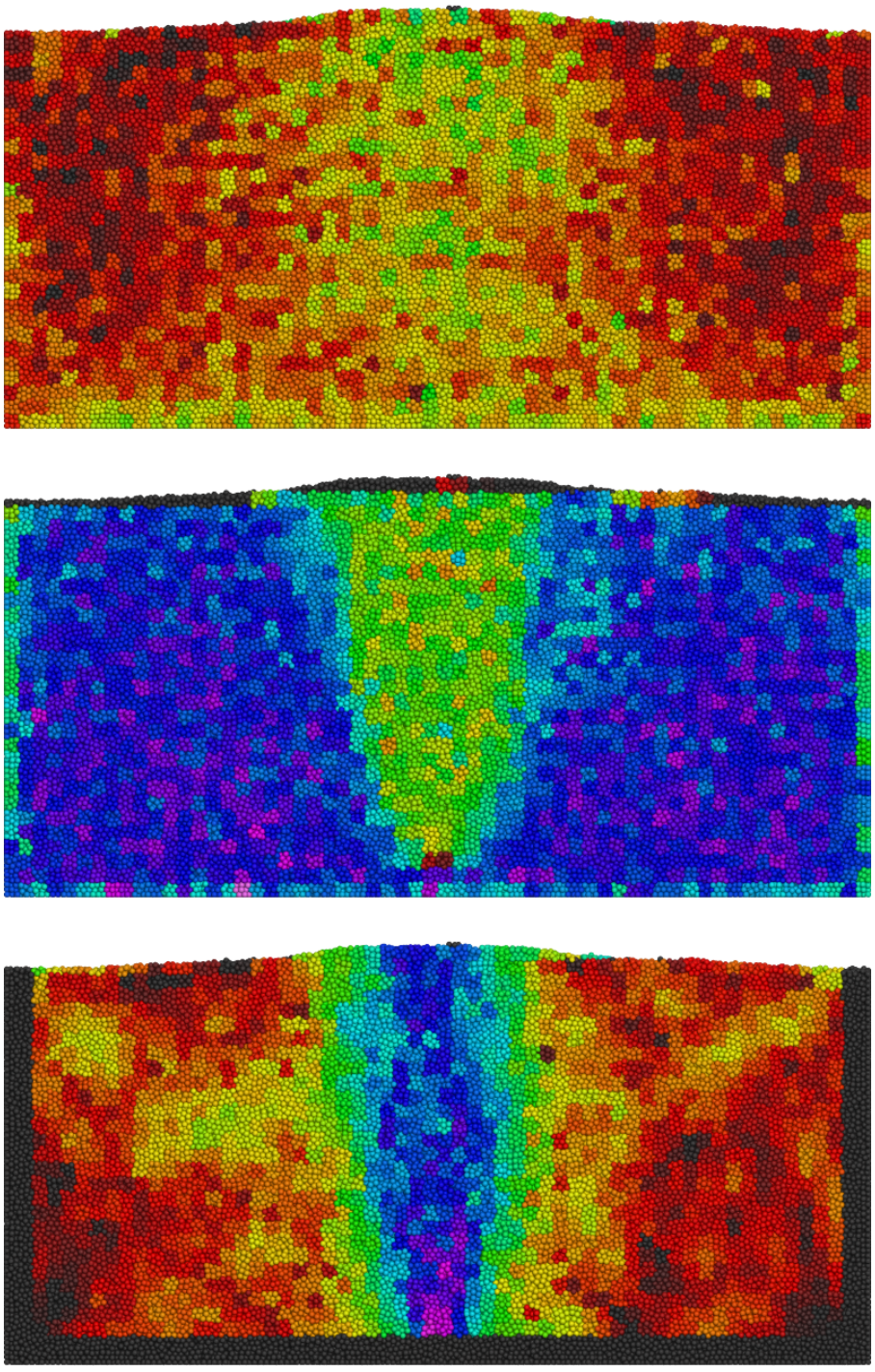

Figure 7-12: Three computed material quantities (μ, top; packing fraction ϕ, middle; magnitude of deviatoric strain rate $|\mathbf{D_0}|$, bottom) in the wide silo shearing simulation at $t = 200\tau$, using the color scheme in figure 7-3.

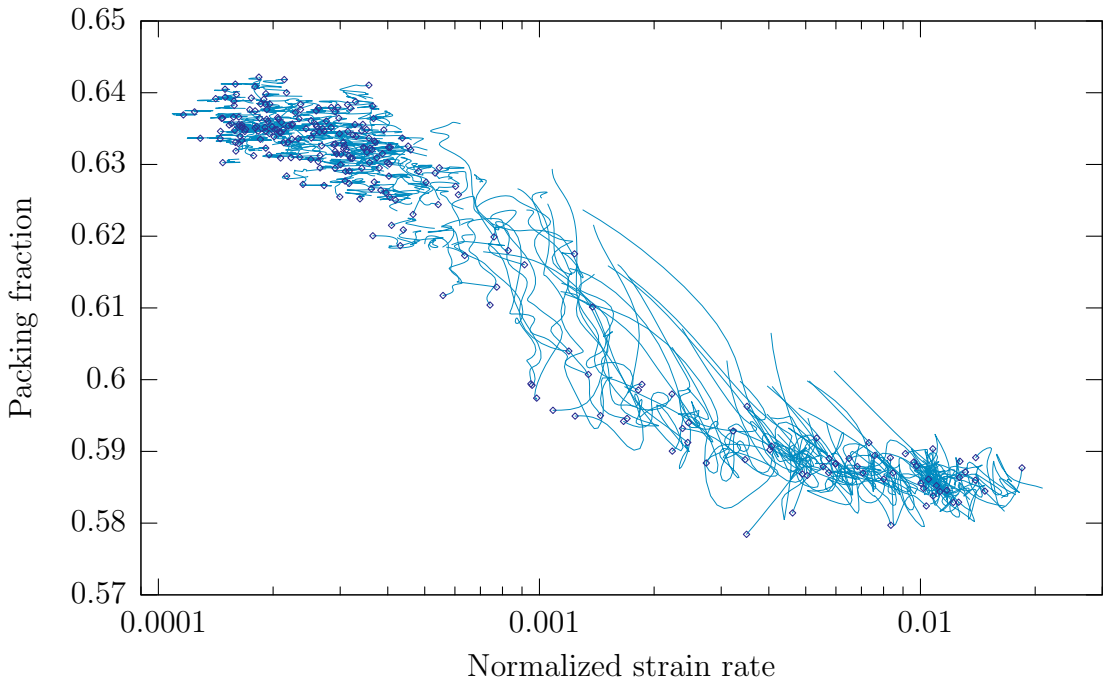

Figure 7-13: Lagrangian tracer plot for strain rate versus packing fraction for the long shearing simulation.

packing fraction, a point of view which has also been expressed in the literature, particularly from an engineering standpoint. Strain and strain rate are very different, and it appears that only one of these connections should exist. The situation is complicated by the fact for a single simulation snapshot, the regions of high strain may be loosely correlated with those of high strain rate.

The shearing experiment discussed in section 7.2 provides the ideal test environment for resolving this paradox. Since each granular element only moves in the y direction, it should experience a constant strain rate, while strain will be constantly increasing. Figure 7-12 shows snapshots of μ, packing fraction, and strain rate in this simulation. To infer long-time behavior, the simulation was run for ten times as long as the other runs, with snapshots saved at intervals of 2τ.

Figures 7-13 and 7-14 show plots of strain rate and strain against packing fraction. In these plots, a distinction has been made between the ends of the tracers (shown in dark blue), and the tracers themselves (shown in light blue). In the strain rate plot, we see that while th tracers are somewhat spread out, the end points are all on

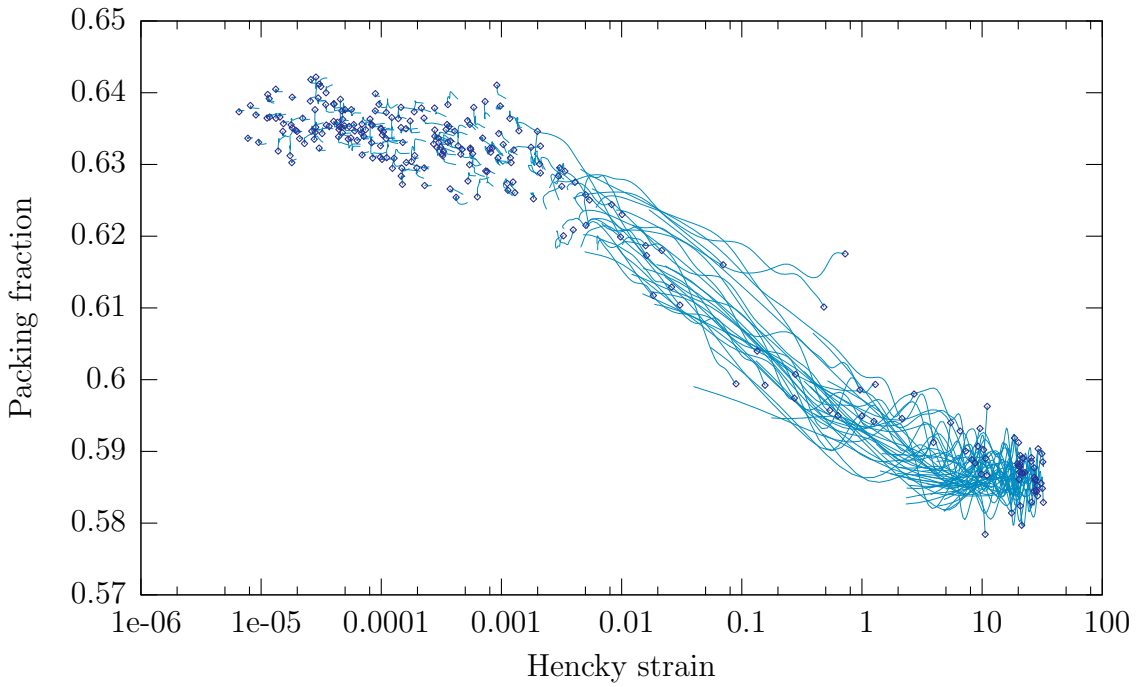

Figure 7-14: Lagrangian tracer plot for strain versus packing fraction for the long shearing simulation.

a fairly tight monotonically decreasing line. This suggests that strain rate may be instrumental in determining the granular material's final packing fraction: any granular element which experiences a constant strain rate for long enough will ultimately end up on this line.

By contrast, in the plot of strain against packing fraction, the tracers, and not the end points, appear to show the best collapse. Coupled with the previous data, this suggests that strain may be instrumental in the dilation process itself, while the final packing fraction will be set. In order for this to be consistent with the previous result, we would expect that some tracers at low strain rates would eventually peel off the main curve of tracers in the strain graph, once they had found their steady state. Testing for this is difficult, since one would have to run the simulation for many times longer. However there are two tracers in figure 7-14 which appear to be starting to peel away.

Looking at different shearing velocities in this system could provide more data to confirm this. Unfortunately, a Lagrangian tracer plot of strain rate against packing in

the drainage and pushing simulations is quite noisy and uninstructive, since it seems that few elements experience a constant shear rate for a long enough time to reach their steady state.

7.7 Conclusion

The above results show that is it possible to make a direct connection between continuum theories and particle-based simulations of dense granular flow at the local level. Motivated by previous work on co-operative particle motion, we have shown that it is possible to define an approximate granular element at the level of several particle diameters, and while material quantities computed at this scale exhibit statistical variation, they are clear enough to provide many insights into the rheology of granular materials.

We have been able to answer a variety of questions about how a granular element will behave, and since our conclusions have been shown for several different simulations, it is hoped that these properties are inherent in the granular material itself, and not tied to any particular geometry. We have tested several of the fundamental ideas behind Mohr-Coulomb plasticity theory, showing that coaxiality appears to be well-satisfied, while the Mohr-Coulomb incipient yield hypothesis appears invalid. However, we have shown that μ still plays a critical role, and we have explicitly demonstrated how it can control failure and dilation.

Consistent with the results of da Cruz [33], we have shown a link between strain rate and packing fraction. However, while their results were carried out in 2D, we have shown this result locally in 3D. Our results also show that while strain rate is important in determining the steady state which a packing will reach, the total strain plays an important role in determining the process by which the deformation takes place.

The above method provides us with an ideal tool for testing and developing continuum theories of granular materials. In the future we hope to directly examine recently proposed ideas in for plasticity theories, such as Pouliquen's flow rule [62].

Examining fully 3D situations may provide useful clues, since it may allow us greater control and variation in the stress tensor. In this work, we only considered yielding as a function of μ, which is defined in terms of the maximum and minimum stress eigenvalue. A useful study would be to check the role, if any, of the intermediate stress eigenvalue, a question which is currently unresolved.

We also hope to make direct connections to other continuum, non-plasticity, theories for granular materials such as STZ theory, or partial fluidization. These theories are frequently characterized by having a microscopic continuum quantity, such as STZ populations $n_{\pm}$ or partial fluidization parameter ρ, and part of the challenge in investigating these parameters will be to understand how they directly relate to the microscopic packing structure. Another promising and related avenue to pursue is to better understand the role of total strain. While strain appeared to play a crucial role in interpreting our data, it is an undesirable quantity to use in an eventual continuum theory of granular materials, since it is always tied to an initial reference state. While granular materials exhibit memory effects, it is also important that they are able to "forget" their initial reference state after a long period of rearrangement.